

Observational Constraints on Southern Ocean Cloud-phase Feedback

Casey James Wall¹, Trude Storelvmo², Joel R. Norris³, and Ivy Tan⁴

¹Scripps Institution of Oceanography

²University of Oslo

³UCSD

⁴McGill University

November 22, 2022

Abstract

Shortwave radiative feedbacks from Southern Ocean clouds are a major source of uncertainty in climate projections. Much of this uncertainty arises from changes in cloud scattering properties and lifetimes that are caused by changes in cloud thermodynamic phase. Here we use satellite observations to infer the scattering component of the cloud-phase feedback mechanism and determine its relative importance by comparing it with an estimate of the overall temperature-driven cloud feedback. The overall feedback is dominated by an optical thinning of low-level clouds. In contrast, the scattering component of cloud-phase feedback is an order of magnitude smaller and is primarily confined to free-tropospheric clouds. The small magnitude of this feedback component is a consequence of counteracting changes in albedo from cloud optical thickening and shifts in the scattering direction of cloud particles. These results indicate that shortwave cloud feedback is likely positive over the Southern Ocean and that changes in cloud scattering properties arising from phase changes make a small contribution to the overall feedback. The feedback constraints shift the projected 66% confidence range for the global equilibrium temperature response to doubling atmospheric CO₂ by about +0.1 K relative to a recent consensus estimate of cloud feedback.

Observational Constraints on Southern Ocean Cloud-phase Feedback

1 Casey J. Wall^{1*}, Trude Storelvmo^{2,3}, Joel R. Norris¹, Ivy Tan⁴

2 ¹Scripps Institution of Oceanography, University of California San Diego, La
3 Jolla, CA, United States

4 ²Department of Geosciences, University of Oslo, Oslo, Norway

5 ³School of Business, Nord University, Bodø, Norway

6 ⁴Department of Atmospheric and Oceanic Sciences, McGill University, Montreal,
7 Canada

8

9 Corresponding Author:

10 Casey J. Wall, cawall@ucsd.edu

11

12 Submitted September 4, 2021

13

14

15

16

17

18

19

20

21

22

23 **Key Points**

24 1. Observations suggest that shortwave cloud-climate feedback is positive
25 over the Southern Ocean

26 2. Changes in cloud scattering properties arising from ice-to-liquid
27 conversions make a small contribution to the feedback

28 3. The observational constraints imply a higher climate sensitivity than a
29 recent consensus estimate of cloud feedback

30 **Abstract**

31 Shortwave radiative feedbacks from Southern Ocean clouds are a major
32 source of uncertainty in climate projections. Much of this uncertainty arises from
33 changes in cloud scattering properties and lifetimes that are caused by changes
34 in cloud thermodynamic phase. Here we use satellite observations to infer the
35 scattering component of the cloud-phase feedback mechanism and determine its
36 relative importance by comparing it with an estimate of the overall temperature-
37 driven cloud feedback. The overall feedback is dominated by an optical thinning
38 of low-level clouds. In contrast, the scattering component of cloud-phase
39 feedback is an order of magnitude smaller and is primarily confined to free-
40 tropospheric clouds. The small magnitude of this feedback component is a
41 consequence of counteracting changes in albedo from cloud optical thickening
42 and shifts in the scattering direction of cloud particles. These results indicate that
43 shortwave cloud feedback is likely positive over the Southern Ocean and that
44 changes in cloud scattering properties arising from phase changes make a small
45 contribution to the overall feedback. The feedback constraints shift the projected
46 66% confidence range for the global equilibrium temperature response to
47 doubling atmospheric CO₂ by about +0.1 K relative to a recent consensus
48 estimate of cloud feedback.

49

50 **Plain Language Summary**

51 Understanding how clouds respond to global warming is a key challenge
52 of climate science. One particularly uncertain aspect of the cloud response
53 involves a conversion of ice particles to liquid droplets in extratropical clouds.
54 Here we use satellite data to infer how ice-to-liquid conversions affect climate by
55 changing the reflection of incoming solar radiation back to space. We find that
56 the changes in cloud particle size and shape that arise from phase changes
57 make a relatively small contribution to the overall cloud-albedo response to
58 warming. This finding provides new insight about how changes in cloud phase
59 affect climate change.

60 **1. Introduction**

61 The Southern Ocean is one of the cloudiest places on Earth. Vast
62 blankets of low clouds cover the region, and streaks of high clouds form from the
63 continuous churning of weather systems. Collectively these clouds have large
64 radiative effects that shape global climate (Hwang and Frierson, 2013; Kay et al.,
65 2016; Hawcroft et al., 2017).

66 Southern Ocean clouds are also susceptible to producing cloud-climate
67 feedbacks that have global consequences. For instance, projections from the
68 Coupled Model Intercomparison Project Phase 6 (CMIP6) predict more positive
69 Southern Ocean cloud feedback and higher climate sensitivity than previous
70 assessments (Zelinka et al., 2020). The CMIP6 projections show that Southern
71 Ocean cloud feedback affects climate sensitivity, but the models have large
72 parametric uncertainties that prevent them from precisely predicting this
73 feedback. Previous observational studies have attempted to constrain the
74 feedback, but they have yet to reach a consensus on sign (Ceppi, McCoy, and
75 Hartmann, 2016; Terai et al., 2016; Lutsko et al., 2021). These results indicate
76 that Southern Ocean clouds exert a potentially powerful but highly uncertain
77 feedback on global climate change.

78 One major component of the feedback uncertainty arises from changes in
79 cloud phase (Storelvmo et al., 2015). As the atmosphere warms, some cloud
80 particles that would have previously been ice will form as liquid instead. These
81 phase conversions change the size and shape of cloud particles, which changes
82 the scattering properties of clouds. Ice-to-liquid conversions also reduce
83 precipitation efficiency, thereby increasing cloud lifetimes. We call these effects
84 the scattering and lifetime components of cloud-phase feedback, respectively.
85 Both are the product of complex interactions among microphysical processes,
86 and thus they are highly uncertain.

87 In this study we use satellite observations to constrain the scattering
88 component of Southern Ocean cloud-phase feedback. Despite the importance of
89 this mechanism in many climate projections (Ceppi, Hartmann, and Webb, 2016;
90 Tan et al., 2016; Frey and Kay, 2018), observational support for the mechanism

91 has been limited to estimates that do not quantify confidence intervals and do not
92 compare the mechanism to the overall cloud feedback to place it into context
93 (McCoy et al., 2014a; Tan et al., 2019). Here we introduce a method to estimate
94 cloud feedback as a function of cloud-top phase, which facilitates stronger
95 constraints. We first estimate the cloud-phase scattering feedback and the
96 overall temperature-mediated cloud feedback, and then we investigate the
97 implications of these feedbacks for climate sensitivity.

98

99 **2. Data and Methods**

100 2.1 Observations and Model Output

101 We extend a method of cloud-feedback analysis developed by Zelinka et
102 al. (2012) to decompose shortwave (SW) feedbacks based on cloud
103 thermodynamic phase. The method is applied to monthly gridded observations
104 from the Moderate Resolution Imaging Spectroradiometer (MODIS) instrument
105 onboard the Aqua satellite (Platnick et al., 2017). MODIS cloud-phase data
106 represent phase at cloud top, and they have a ~90% frequency of agreement
107 with lidar data, which are the most accurate phase retrievals from space (Huang
108 et al., 2016; Marchant et al., 2016). We analyze cloud-fraction histograms
109 partitioned by cloud-top pressure (CTP), optical depth (τ), and phase (Fig. 1a-b).
110 The standard liquid- and ice-cloud histograms have different CTP- τ bins, so
111 some adjacent bins are merged to make the intervals similar. In this step, clouds
112 with CTP > 1000 hPa are reassigned to the 800-1000 hPa bin, and it is assumed
113 that no liquid clouds exist between 50-150 hPa. The standard and modified bin
114 boundaries are listed in Table S1.

115 We also analyze monthly meteorological data and sea-ice area fraction
116 from ERA5 reanalysis (Hersbach et al., 2020). Three-dimensional temperature,
117 horizontal wind, and vertical wind fields are linearly interpolated to the MODIS
118 grid and to pressure intervals corresponding to the MODIS CTP bins. We also
119 calculate estimated inversion strength, which represents the inversion at the top
120 of the boundary layer (Wood and Bretherton, 2006). The observations and
121 reanalysis data are analyzed between 40°-60°S and from 2003-2019, unless

122 stated otherwise, and the analysis is restricted to ocean gridboxes with monthly
123 sea-ice cover below 1%.

124 We also use output from 34 CMIP6 global climate models to represent
125 CO₂-forced warming (Table S2). Model simulations are run for 150 years
126 following an abrupt quadrupling of atmospheric CO₂ concentrations relative to
127 preindustrial values (“abrupt4xCO₂” experiment). Atmospheric temperatures are
128 linearly interpolated to the MODIS grid and CTP intervals, and then they are
129 averaged over the final 30 years of the simulations. Averages are calculated
130 separately for each latitude, calendar month, and CTP interval. To remove model
131 drift, the temperature response to increasing CO₂ is calculated by subtracting the
132 preindustrial integration (“piControl”) from the corresponding parallel
133 abrupt4xCO₂ integration. The response of global-mean near-surface air
134 temperature is calculated similarly. Only the first ensemble member from each
135 model is used.

136

137 2.2 Radiative Kernels

138 Cloud-fraction anomalies from each MODIS histogram bin are converted
139 into top-of-atmosphere SW flux anomalies using radiative kernels. The kernels
140 represent how much a unit cloud-fraction change modifies top-of-atmosphere SW
141 flux with all non-cloud factors fixed at climatological values. We calculate the
142 kernels as a function of latitude, longitude, and calendar month following the
143 method of Zelinka et al. (2012), except that we generalize their framework by
144 calculating separate kernels for liquid and ice clouds. The calculations are
145 performed using the Rapid Radiative Transfer Model for GCMs (Clough et al.,
146 2005) with climatological seasonal cycles of humidity from ERA5 and surface
147 albedo from Clouds and the Earth’s Radiant Energy System satellite
148 observations (Loeb et al., 2018). We also change the mean cloud-droplet
149 effective radius and ice-crystal effective radius to 14 μm and 35 μm , respectively,
150 to match observed values over the Southern Ocean (McCoy et al., 2014a).
151 Together the cloud histograms and kernels reproduce observed variations of SW
152 cloud radiative effects with an error of ~5% (Appendix A).

153 Fig. 1c-d shows the spatial and temporal average of the radiative kernels.
 154 The kernels have negative values because a larger cloud fraction increases SW
 155 reflection to space. They depend relatively strongly on τ , and they depend
 156 weakly on CTP because of SW absorption by water vapor. For a given CTP- τ
 157 combination, the kernels also depend on cloud phase because ice particles
 158 typically backscatter more radiation than liquid droplets (Stackhouse and
 159 Stephens, 1991). Changes in any of these cloud properties can therefore
 160 contribute to cloud feedback.

161

162 2.3 Feedback Analysis

163 The MODIS histograms and kernels are leveraged to estimate the SW
 164 cloud feedback that is directly caused by atmospheric warming. We do not
 165 consider SW feedbacks caused by shifts in large-scale circulation because they
 166 are thought to be relatively small (Ceppi and Hartmann, 2015). Let i represent
 167 any bin in the liquid- or ice-cloud histogram. For a given location and calendar
 168 month, the SW feedback from clouds in bin i is

$$F_{SW,i} = \frac{\partial c_i}{\partial T_i} K_i \frac{dT_i}{dT_{2m}} \quad (1)$$

169 where c_i is cloud fraction, T_i is temperature at the location and vertical level of bin
 170 i , K_i is the corresponding element of the kernel, and T_{2m} is global-mean surface
 171 air temperature. On the right side of equation 1, the first term is the cloud
 172 response to local warming, the second term converts the cloud response into
 173 top-of-atmosphere SW flux, and the third term relates local warming to global-
 174 mean surface warming. All temperature-dependent terms represent the response
 175 to an external climate forcing. The task of quantifying cloud feedback thus
 176 reduces to estimating these terms.

177 We first calculate dT_i/dT_{2m} , which represents the magnitude and vertical
 178 structure of atmospheric warming over the Southern Ocean relative to global-
 179 mean surface warming. This term is calculated from the CMIP6 projections
 180 forced by increasing atmospheric CO₂. The projections of dT_i/dT_{2m} consistently
 181 have maximum values in the free troposphere and smaller values in the lower

182 stratosphere and near the surface (Fig. 2). Small stratospheric values are a
 183 consequence of larger emissivity from enhanced CO₂ concentrations (Hartmann,
 184 2016), and small near-surface values are a consequence of upwelling ocean
 185 currents (Armour et al., 2016). These physical explanations and the consistency
 186 among models suggest that the projections of dT_i/dT_{2m} are robust.

187 The feedback analysis also requires estimates of $\partial c_i/\partial T_i$. This term
 188 represents the temperature-driven cloud response to a climate forcing, but it can
 189 be estimated from natural variability assuming that cloud-temperature
 190 relationships will not substantially change as the climate evolves. This
 191 assumption neglects the potential dependence of extratropical cloud feedbacks
 192 on the climate state (Bjordal et al., 2020). However, many climate projections
 193 suggest that monthly cloud-temperature relationships from natural variability
 194 accurately predict extratropical cloud feedbacks (Tselioudis et al., 1998; Gordon
 195 and Klein, 2014; Terai et al., 2016; Ceppi, McCoy, and Hartmann, 2016), and
 196 observed cloud-temperature relationships are similar in different epochs within
 197 the MODIS record (Appendix C). We therefore estimate $\partial c_i/\partial T_i$ from natural
 198 variability.

199 We first estimate $\partial c_i/\partial T_i$ associated with the temperature-mediated
 200 feedback. This term represents the overall cloud response to warming, and it is
 201 calculated using multilinear regression. Because of the zonal symmetry of the
 202 Southern Ocean, regression is performed on data from all longitude points
 203 simultaneously. The climatological seasonal cycle is removed from each latitude-
 204 longitude gridbox, and data are composited by latitude and calendar month. For
 205 each latitude, month, and histogram bin, we calculate a regression model of the
 206 form

$$c = \sum_{n=1}^N \frac{\partial c}{\partial x_n} x_n + \epsilon \quad (2)$$

207 where x_n are meteorological predictors, $\partial c/\partial x_n$ are regression coefficients, N is
 208 the number of meteorological predictors, and ϵ is the residual. The
 209 meteorological predictors include temperature and the three-dimensional wind
 210 field at the level of the CTP interval. Estimated inversion strength is also used as

211 a predictor for CTP > 450 hPa. The term $\partial c/\partial T$ therefore represents the cloud
 212 response to warming while controlling for wind and inversion strength. On
 213 average, the regression model explains 38% of the variance of cloud-induced
 214 SW flux anomalies for boundary layer clouds (CTP > 800 hPa) and 18% of the
 215 variance for tropopause-level clouds ($250 \text{ hPa} < \text{CTP} \leq 350 \text{ hPa}$). The explained
 216 variance for boundary layer clouds is similar to that of other observational work
 217 that uses different meteorological predictors (Scott et al., 2020). This suggests
 218 that the regression model represents cloud-meteorology relationships with skill
 219 that is similar to other available methods. Ultimately the cloud-temperature
 220 regression coefficients are used to estimate the temperature-mediated feedback
 221 following equation 1.

222 We also estimate the component of the temperature-mediated feedback
 223 that arises from changes in low-cloud optical depth. We define low clouds by
 224 CTP > 600 hPa, and we apply the method of Scott et al. (2020) to decompose
 225 low-cloud fraction anomalies into a component from anomalous cloud amount
 226 and a component from anomalous cloud optical properties and CTP. The latter
 227 component is regressed on the meteorological predictors to estimate the
 228 associated SW feedback. This feedback component is dominated by shifts in
 229 optical depth, so we henceforth call it the low-cloud optical depth feedback.

230 The values of $\partial c_i/\partial T_i$ associated with the scattering component of cloud-
 231 phase feedback are estimated from a different procedure. We calculate these
 232 terms separately for each CTP bin so that phase conversions happen between
 233 clouds at the same vertical level. For a given CTP bin, the proportion of clouds
 234 that are liquid is

$$235 \quad P_{liq} = \frac{C_{liq}}{C_{liq} + C_{ice}}$$

236 where C_{liq} and C_{ice} are the total liquid- and ice-cloud fractions in the CTP bin. P_{liq}
 237 is regressed on the meteorological predictors as in equation 2 to calculate
 238 $\partial P_{liq}/\partial T$, where T is temperature in the CTP interval. Changes in C_{liq} and C_{ice}
 239 with warming are determined by

$$240 \quad \frac{\partial C_{liq}}{\partial T} = \frac{\partial P_{liq}}{\partial T} (\overline{C_{liq}} + \overline{C_{ice}})$$

$$241 \quad \frac{\partial C_{ice}}{\partial T} = -\frac{\partial P_{liq}}{\partial T} (\overline{C_{liq}} + \overline{C_{ice}})$$

242 where overbars indicate values from the climatological seasonal cycle. $\partial C_{liq}/\partial T$
 243 and $\partial C_{ice}/\partial T$ are equal and opposite, so they represent a phase change with
 244 fixed overall cloud fraction. The values of $\partial C_{liq}/\partial T$ and $\partial C_{ice}/\partial T$ are then
 245 distributed among the τ bins in proportion to the climatological distributions:

$$246 \quad \frac{\partial c_{liq,k}}{\partial T} = \frac{\partial C_{liq}}{\partial T} \frac{\overline{c_{liq,k}}}{\overline{C_{liq}}}$$

$$247 \quad \frac{\partial c_{ice,l}}{\partial T} = \frac{\partial C_{ice}}{\partial T} \frac{\overline{c_{ice,l}}}{\overline{C_{ice}}}$$

248 where $c_{liq,k}$ and $c_{ice,l}$ are the liquid- and ice-cloud fractions in τ bins k and l ,
 249 respectively. By distributing cloud fraction this way we are assuming that for any
 250 latitude-month-CTP bin, all ice clouds in the bin have the same probability of
 251 undergoing a phase change. Ultimately $\partial c_{liq,k}/\partial T$ and $\partial c_{ice,l}/\partial T$ are used to
 252 calculate the cloud-phase scattering feedback following equation 1. An example
 253 of this procedure is presented in the Supporting Information.

254 The cloud-phase scattering feedback is also decomposed into
 255 contributions from changes in different optical properties. The total cloud-phase
 256 scattering feedback for a given latitude, month, and CTP bin is

$$257 \quad \hat{F}_{SW,phase} = \frac{dT}{dT_{2m}} \left(\sum_{l=1}^9 \frac{\partial c_{ice,l}}{\partial T} K_{ice,l} + \sum_{k=1}^9 \frac{\partial c_{liq,k}}{\partial T} K_{liq,k} \right)$$

258 where K_{ice} and K_{liq} are the ice- and liquid-cloud kernels and the sums are
 259 performed over the τ dimension. Let K_{liq}^* represent the liquid-cloud kernel
 260 evaluated on the ice-cloud τ bins. The feedback can then be expressed as

$$261 \quad \hat{F}_{SW,phase} = \left[\frac{dT}{dT_{2m}} \sum_{l=1}^9 \frac{\partial c_{ice,l}}{\partial T} (K_{ice,l} - K_{liq,l}^*) \right]$$

$$262 \quad + \left[\frac{dT}{dT_{2m}} \left(\sum_{l=1}^9 \frac{\partial c_{ice,l}}{\partial T} K_{liq,l}^* + \sum_{k=1}^9 \frac{\partial c_{liq,k}}{\partial T} K_{liq,k} \right) \right].$$

263 The first term in square brackets is determined by the difference between the
 264 liquid- and ice-cloud kernels, so it represents the feedback component from
 265 changes in scattering direction and the relative importance of scattering and
 266 absorption. These properties are represented by the cloud-particle asymmetry
 267 parameter g and single-scattering albedo $\tilde{\omega}$, respectively. The second term in
 268 square brackets is determined by the difference between $\partial c_{ice}/\partial T$ and $\partial c_{liq}/\partial T$.
 269 Since $\partial c_{ice}/\partial T$ and $\partial c_{liq}/\partial T$ have opposite sign and sum to zero when adding
 270 over all τ bins, this feedback component represents changes in the overall optical
 271 depth distribution that are caused by phase changes.

272 All feedbacks are calculated for every latitude-month combination, except
 273 when high solar zenith angle limits the number of observations. To ensure that
 274 the cloud histograms are adequately sampled, we require that each gridbox has
 275 at least 500 valid MODIS pixels, which is 6-7% of spring and summer values.
 276 This condition is not satisfied poleward of 56°S in June and poleward of 59°S in
 277 July. In these cases, regression slopes are taken from the same latitude and the
 278 closest calendar month with sufficient data. If two months are equally close, then
 279 the average of their regression slopes is used. The feedbacks are averaged over
 280 the seasonal cycle and latitude, weighting by ocean area. Feedback uncertainty
 281 is represented by 95% confidence intervals that account for uncertainty in
 282 observed cloud-temperature relationships, uncertainty in cloud microphysical
 283 properties assumed when calculating the kernels, and inter-model spread in
 284 projections of dT_i/dT_{2m} (Appendix B).

285

286 **3. Southern Ocean Cloud Feedback**

287 We next compare the cloud-phase scattering feedback to the overall
 288 temperature-mediated feedback over the Southern Ocean. Fig. 3 shows the
 289 feedback components as a function of CTP, τ , and phase. The temperature-
 290 mediated feedback includes a vertical dipole pattern from rising upper-
 291 tropospheric ice clouds (Fig. 3a). This is qualitatively consistent with established
 292 energetic constraints: The average depth of the troposphere is limited to levels
 293 with appreciable clear-sky radiative cooling, which is constrained to temperatures

294 warmer than ~220 K by the nature of the water-vapor rotation bands (Thompson
295 et al., 2017; Jeevanjee and Fueglistaler, 2020). Thus, as the atmosphere warms
296 and isotherms rise, the highest ice clouds rise as well. A second dipole pattern
297 shows that the top of low-level liquid clouds sinks as the atmosphere warms (Fig.
298 3b). This cloud response has been reported in other satellite and field
299 observations, but the physical cause is not fully understood (Huang et al., 2016;
300 Mace et al., 2021). One possibility is that a warmer, more emissive free
301 troposphere reduces cloud-top radiative cooling. This weakens turbulence and
302 reduces the vertical development of boundary layer clouds (Eastman and Wood,
303 2018).

304 In contrast to the temperature-mediated feedback, the cloud-phase
305 scattering feedback has a strikingly different pattern (Fig. 3c-d). Throughout the
306 troposphere the ice-cloud feedback is positive and the liquid-cloud feedback is
307 negative, indicating an ice-to-liquid conversion. The feedback magnitude
308 maximizes in the middle troposphere, where ice and liquid clouds both occur
309 (Fig. 1a-b). It is not obvious from Fig. 3 how much the cloud-phase scattering
310 feedback contributes to the total temperature-mediated feedback, but it is clear
311 that other feedback mechanisms contribute as well.

312 The temperature-mediated and cloud-phase feedbacks can be compared
313 more clearly by summing the components over the CTP dimension to remove
314 dipole signals from vertical shifts in clouds. The prevailing signal of the
315 temperature-mediated feedback for low-level clouds (CTP > 600 hPa) is an
316 optical thinning of liquid cloud (Fig. 4a-b). Previous work suggests that this
317 positive low-cloud optical depth feedback could be a consequence of reduced
318 cloud-top radiative cooling, more frequent decoupling of clouds from the surface
319 mixed layer, or more efficient drying from cloud-top entrainment (Terai et al.,
320 2019; Mace et al., 2021). Our results do not speak to the physical cause, but they
321 do show that the cumulative effect of positive feedback mechanisms outweighs
322 that of negative feedback mechanisms, including enhanced condensation in
323 saturated updrafts and cloud-phase changes (Betts and Harshvardhan, 1987;
324 Lutsko and Cronin, 2018). Indeed, the scattering component of cloud-phase

325 feedback is negligible for low clouds because ice clouds rarely occur at this level
326 (Fig. 4d-e; Fig. 1).

327 In contrast, the feedback from non-low clouds ($CTP \leq 600$ hPa) has
328 different characteristics. The temperature-mediated feedback includes an ice-to-
329 liquid conversion, and the cloud-phase scattering feedback has the same sign
330 but larger magnitude (Fig. 4). This difference in magnitude may be associated
331 with non-low clouds shifting upward as the atmosphere warms (Fig. 3a). As
332 clouds shift upward they experience less warming and therefore a reduced ice-
333 to-liquid conversion compared to what would occur if they were to remain at fixed
334 altitudes. The estimate of cloud-phase scattering feedback represents phase
335 conversions with fixed cloud altitudes, while the estimate of temperature-
336 mediated feedback includes the effect of upward shifts in clouds. Despite this
337 difference, the results consistently show that the cloud-phase scattering feedback
338 is primarily confined to free-tropospheric clouds.

339 We next sum the feedback components over the optical depth dimension
340 to determine the total feedback. Low clouds exert a significant positive
341 temperature-mediated feedback that mostly arises from liquid clouds, and non-
342 low clouds exert counteracting ice and liquid feedbacks that sum to a near-zero
343 value (Fig. 4c). The low-cloud component is largest, and thus the total feedback
344 is positive (Fig. 5a). Low clouds dominate the mean cloud albedo over the
345 Southern Ocean, so it is perhaps not surprising that they dominate the
346 temperature-mediated feedback as well (Haynes et al., 2011). In contrast, the
347 cloud-phase scattering feedback is mostly limited to non-low clouds, and it
348 consists of ice and liquid components that cancel very closely (Fig. 4f, Fig. 5a).
349 The total temperature-mediated feedback summed over all CTP- τ -phase
350 components is significantly positive ($0.65 \pm 0.32 \text{ Wm}^{-2}\text{K}^{-1}$) and is an order of
351 magnitude larger than the total cloud-phase scattering feedback (-0.02 ± 0.05
352 $\text{Wm}^{-2}\text{K}^{-1}$). Thus, changes in cloud scattering properties arising from phase
353 changes make a small contribution to the overall temperature-driven cloud
354 feedback.

355 The smallness of the cloud-phase scattering feedback is surprising given
356 that it can be much larger in model simulations (Ceppi, Hartmann, and Webb,
357 2016; Tan et al., 2016; Frey and Kay, 2018). To interpret this result, we
358 decompose the feedback into contributions from changes in (1) optical depth; (2)
359 single-scattering albedo $\tilde{\omega}$, which is the probability that a photon-particle
360 interaction results in scattering; and (3) asymmetry parameter g , which embodies
361 scattering direction. The decomposition reveals that phase changes cause a
362 negative optical depth feedback (Fig. 5b). This is consistent with the expectation
363 that ice-to-liquid conversions reduce the average size of cloud particles, thereby
364 increasing particle surface-area-to-volume ratio and hence the bulk optical depth.
365 The decomposition also reveals an offsetting positive feedback from changes in
366 g and $\tilde{\omega}$. This component is mostly caused by changes in scattering direction: Ice
367 particles typically backscatter more radiation than liquid droplets, so ice-to-liquid
368 conversions enhance forward scattering and thereby reduce cloud albedo. The
369 magnitude of this feedback component may be somewhat sensitive to the
370 microscopic properties of cloud particles that are assumed when calculating the
371 kernels, but the confidence intervals account for much of this uncertainty by
372 incorporating particle-size uncertainty and using two radiative transfer schemes
373 (Appendix B). The main interpretation is therefore robust: Ice-to-liquid
374 conversions increase cloud optical depth and shift the scattering angles of cloud
375 particles toward the forward direction. These counteracting feedback
376 components make the overall cloud-phase scattering feedback small.

377 All of these feedback values are inferred from observed natural variability,
378 so they are contingent on the assumptions of the methodology and the limitations
379 of the observations. However, we tested the sensitivity of the results to the most
380 salient of these assumptions and limitations. For instance, the radiative kernel
381 method assumes that clouds are either entirely liquid or entirely ice (Zelinka et
382 al., 2012) based on observed cloud-top phase. Sensitivity to this assumption is
383 tested by matching MODIS pixels with coincident radar-lidar measurements to
384 distinguish ice, pure liquid, and mixed-phase clouds, then estimating the cloud-
385 phase scattering feedback while allowing for transitions between the three phase

386 categories. We also checked sensitivity to satellite retrieval bias from high solar
387 zenith angle and multilayer clouds, and we checked sensitivity to observing
388 platform and time period. The envelope of feedback uncertainty from the
389 sensitivity tests is close to that of the main estimates (Appendix C). Thus, these
390 assumptions and limitations do not affect the main results.

391

392 **4. Implications for Climate Sensitivity**

393 We next frame the results in the context of the existing literature to show
394 their implications for climate sensitivity. A recent survey by Sherwood et al.
395 (2020) identified high-latitude (40°-70°) low-cloud optical depth feedback as one
396 of six primary components of global cloud feedback. Observational studies have
397 argued that this feedback component could be positive (Tselioudis et al., 1992;
398 Norris and Iacobellis, 2005; Huang et al., 2016; Terai et al., 2016; Tan et al.,
399 2019; Mace et al., 2021; Myers et al., 2021) or negative (McCoy et al., 2014b;
400 Ceppi, McCoy, and Hartmann, 2016). Sherwood et al. (2020) therefore
401 established a consensus estimate with a central value of $0 \text{ Wm}^{-2}\text{K}^{-1}$ and a
402 confidence interval wide enough to include positive and negative feedback
403 values estimated by Terai et al. (2016) and Ceppi, McCoy, and Hartmann (2016).
404 The consensus feedback was then combined with other evidence to estimate
405 global cloud feedback and the equilibrium response of global-mean surface
406 temperature to doubling atmospheric CO_2 . The temperature response was
407 represented by effective climate sensitivity (Gregory et al., 2004).

408 Our findings support a different interpretation of high-latitude low-cloud
409 optical depth feedback. First, we find that the feedback is positive over the
410 Southern Ocean ($0.52 \pm 0.23 \text{ Wm}^{-2}\text{K}^{-1}$ over ice-free ocean between 40°-70°S).
411 Second, we find that the negative feedback estimate on which the consensus
412 value is based is probably biased because it does not control for the confounding
413 influence of wind and boundary layer inversion strength (Appendix C). Third, our
414 results rule out the possibility of a substantial negative optical depth feedback
415 from phase changes in Southern Ocean low clouds (Fig. 4). Collectively these

416 findings indicate that high-latitude low-cloud optical depth feedback is likely
417 positive.

418 We investigate the global implications of this result using the framework of
419 Sherwood et al. (2020). Following their analysis, we assume that the high-latitude
420 low-cloud optical depth feedback in the Southern Hemisphere is dominated by
421 ocean regions and is 3.8 times larger than the corresponding feedback in the
422 Northern Hemisphere. These assumptions are based on the analysis of Terai et
423 al. (2016). We then estimate effective climate sensitivity by performing the
424 “Baseline” calculation of Sherwood et al. (2020) with our estimate of high-latitude
425 low-cloud optical depth feedback in place of their consensus value. Our feedback
426 constraint slightly narrows the probability distribution of global cloud feedback,
427 and it increases the modal value from $0.45 \text{ Wm}^{-2}\text{K}^{-1}$ to $0.55 \text{ Wm}^{-2}\text{K}^{-1}$ (Fig. 6a).
428 Consequently, the 66% confidence range for climate sensitivity increases from
429 2.55-3.88 K to 2.63-4.02 K (Fig. 6b). Our observational constraint thus shifts the
430 bounds of the “likely” range of climate sensitivity by about +0.1 K.

431

432 **5. Conclusion**

433 Southern Ocean clouds have large radiative effects that shape global
434 (Hwang and Frierson, 2013; Kay et al., 2016; Hawcroft et al., 2017). They are
435 also especially difficult to simulate, so observations offer a valuable alternative
436 path toward understanding their radiative feedbacks (Trenberth and Fasullo,
437 2010). Here we use MODIS observations to infer Southern Ocean SW cloud
438 feedback as a function of cloud-top phase. The temperature-mediated feedback
439 includes contributions from an optical thinning of low clouds and an ice-to-liquid
440 conversion in free-tropospheric clouds (Fig. 3, Fig. 4). The low-cloud feedback
441 dominates, causing the overall temperature-mediated feedback to be positive
442 (Fig. 5). These constraints imply a higher climate sensitivity than a recent
443 consensus estimate of cloud feedback (Fig. 6).

444 In addition to constraining SW cloud feedback, another key goal is to
445 decompose the feedback into contributions from particular physical mechanisms.
446 Such a decomposition is essential for understanding the climate response to

447 external forcing. Here we leverage the new feedback methodology to isolate one
 448 mechanism: the cloud-phase scattering feedback. This mechanism increases
 449 cloud optical depth and shifts the scattering angles of cloud particles toward the
 450 forward direction. The resulting feedback components closely cancel, and thus
 451 the cloud-phase scattering feedback is an order of magnitude smaller than the
 452 overall temperature-mediated feedback (Fig. 5). These results do not preclude
 453 the possibility of a substantial cloud-phase feedback from cloud-lifetime changes
 454 (Mülmenstädt et al., 2021), nor do they reveal which mechanisms dominate the
 455 temperature-mediated feedback. However, the results do reveal a robust
 456 constraint on Southern Ocean cloud feedback: Although the dominant feedback
 457 mechanisms remain elusive, it is very unlikely that the cloud-phase scattering
 458 feedback is one of them.

459

460 **Appendix A: Validation of Radiative Kernels**

461 SW cloud radiative effect (CRE) is defined as the difference between all-
 462 sky and clear-sky SW flux at the top of the atmosphere. We validate the radiative
 463 kernels by using them to predict monthly anomalies of SW CRE:

$$SW\ CRE_{kernel} = \sum_i c_i K_i \quad (3)$$

464 where i runs over all MODIS histogram bins, c_i is the monthly cloud-fraction
 465 anomaly reported by MODIS, and K_i is the kernel. $SW\ CRE_{kernel}$ is compared with
 466 observed values from Clouds and the Earth's Radiant Energy System satellite
 467 data ($SW\ CRE_{CERES}$; Loeb et al. 2018). Monthly SW CRE anomalies are
 468 averaged over one-year intervals for consistency with the annual-mean SW
 469 cloud-feedback estimates, and $SW\ CRE_{kernel}$ is regressed on $SW\ CRE_{CERES}$
 470 using all data from the study domain. The regression agrees very well with
 471 conditional means of $SW\ CRE_{kernel}$ as a function of $SW\ CRE_{CERES}$, indicating that
 472 linear regression accurately represents bias of the kernel method (Fig. A1). If m
 473 is the regression slope, then $m - 1$ is the bias of the magnitude of $SW\ CRE_{kernel}$.
 474 We find that $m = 1.05 \pm 0.04$ (95% confidence interval). This indicates that the
 475 kernels will overestimate the magnitude of SW cloud feedback by $5 \pm 4\%$.

476

477 **Appendix B: Uncertainty**

478 Cloud feedback is inferred from observed cloud-temperature relationships,
 479 radiative kernels, and model projections of CO₂-forced warming, so all three
 480 terms contribute to feedback uncertainty. These uncertainty components are
 481 independent, so they are calculated separately and then combined. We illustrate
 482 the uncertainty analysis by describing the calculation of the 95% confidence
 483 interval for the mean temperature-mediated feedback for both phases.

484 The first source of feedback uncertainty arises from uncertainty in cloud-
 485 temperature regression slopes. For a given latitude and month, the standard
 486 error of the feedback summed over all MODIS histogram bins is estimated by

$$487 \quad \delta = \sqrt{\sum_i \sum_j \left(\sigma_i K_i \frac{dT_i}{dT_{2m}} \right) \left(\sigma_j K_j \frac{dT_j}{dT_{2m}} \right) r_{i,j}}$$

488 where i and j run over all histogram bins; σ_i is the standard error of regression
 489 slope $\partial c_i / \partial T_i$; $r_{i,j}$ is the correlation between cloud fraction in bins i and j ; and
 490 dT/dT_{2m} is the CMIP6 multi-model mean value. The δ terms are combined to
 491 account for averaging over the seasonal cycle:

$$492 \quad \langle \delta \rangle = \frac{1}{12} \sqrt{\sum_m \delta_m^2}$$

493 where m runs over all calendar months. The $\langle \delta \rangle$ terms are then combined further
 494 to account for averaging over latitude:

$$495 \quad \delta = \sqrt{\sum_l \langle \delta \rangle_l^2 w_l^2 / \sum_l w_l}$$

496 where l runs over all latitude bins and w_l is a weighting factor that is proportional
 497 to ocean area in bin l . Finally, the confidence interval is scaled to account for the
 498 effective degrees of freedom. Serial correlation is diagnosed from SW CRE as
 499 defined by equation (3). The ratio of nominal to effective spatial degrees of
 500 freedom, N_s/N_s^* , is calculated from equation 5 of Bretherton et al. (1999), and the
 501 ratio of nominal to effective temporal degrees of freedom is estimated by

502
$$N_t/N_t^* = \frac{1+r}{1-r}$$

503 where r is the lag-1 autocorrelation of SW CRE. N_t/N_t^* is calculated for every
504 spatial gridpoint and then averaged. The 95% confidence interval for the mean
505 feedback due to regression-slope uncertainty is

506
$$\Delta_1 = \beta \delta \sqrt{\frac{N_s N_t}{N_s^* N_t^*}}$$

507 where β is the critical value of a Student's t test at the 95% confidence level
508 using $N_s^* N_t^* - 6$ degrees of freedom.

509 The second source of uncertainty arises from cloud microphysical
510 properties assumed when calculating the radiative kernels. We assume a mean
511 and 95% confidence interval for cloud-droplet effective radius of $14 \pm 3 \mu\text{m}$,
512 which spans the range of values throughout the climatological seasonal cycle
513 from three MODIS-derived products (McCoy et al., 2014a). We also assume a
514 mean and 95% confidence interval for ice-crystal effective radius of $35 \pm 10 \mu\text{m}$
515 based on satellite radar-lidar observations (McCoy et al., 2014a). Finally, we use
516 two ice optical property schemes that are based on different observed particle-
517 size distributions (Fu, 1996; Ebert and Curry, 1992). Radiative kernels are
518 calculated with the upper and lower bounds of particle size and with both ice
519 optical property schemes, and feedbacks are recalculated with the modified
520 kernels. Variations in feedback values from the kernel modifications are added in
521 quadrature to determine their cumulative contribution to cloud-feedback
522 uncertainty, Δ_2 .

523 The final source of uncertainty arises from the spread in model projections
524 of CO₂-forced warming. To estimate this uncertainty we calculate feedbacks with
525 dT/dT_{2m} from each of the 34 CMIP6 models. The second-largest and second-
526 smallest feedback values are used as bounds for the 95% confidence interval,
527 Δ_3 .

528 After computing the three uncertainty terms, the 95% confidence interval
529 for the mean temperature-mediated feedback Δ_{net} is calculated by adding the
530 terms in quadrature:

531
$$\Delta_{net} = \sqrt{\Delta_1^2 + \Delta_2^2 + \Delta_3^2}.$$

532 Confidence intervals for other feedback components are calculated similarly.

533

534 **Appendix C: Bias**

535 Here we investigate sensitivity of the results to several assumptions of the
 536 methodology and limitations of the observations. We consider the meteorological
 537 predictors used in the regression model, the time period of analysis, and the
 538 observing platform. We also investigate satellite retrieval bias from high solar
 539 zenith angle, multilayer clouds, liquid-topped mixed-phase clouds, and partly
 540 cloudy pixels. The sensitivity tests are described below and summarized in Fig.
 541 A2.

542

543 *Meteorological Predictors*

544 Three studies including ours have reported estimates and confidence
 545 intervals for Southern Ocean SW cloud feedback inferred from MODIS data.
 546 Terai et al. (2016, hereafter T16) estimated that the mean SW low-cloud optical
 547 depth feedback between 40°-70°S is $0.38 \pm 0.25 \text{ Wm}^{-2}\text{K}^{-1}$; Ceppi, McCoy, and
 548 Hartmann (2016, hereafter CMH16) estimated that the mean temperature-
 549 mediated feedback between 45°-60°S is $-0.76 \pm 0.82 \text{ Wm}^{-2}\text{K}^{-1}$ relative to local
 550 warming between 500-850 hPa; and we estimate that the mean temperature-
 551 mediated feedback between 40°-60°S is $0.65 \pm 0.32 \text{ Wm}^{-2}\text{K}^{-1}$. The results of our
 552 study and of T16 are consistent with one another, and both are inconsistent with
 553 the results of CMH16. Here we attempt to reconcile this discrepancy.

554 One difference among the studies is that each one treats confounding
 555 meteorological factors differently. Our study controls for the monthly three-
 556 dimensional wind field and boundary-layer inversion strength. T16 include
 557 changes in inversion strength in their feedback estimate and screen the data for
 558 low clouds, which controls for most of the confounding influence of large-scale
 559 vertical motion. CMH16 do not control for potential confounding factors. To check
 560 if this matters, we align our analysis with that of CMH16 by estimating feedbacks
 561 using only temperature as a predictor. The temperature-only model predicts a

562 SW temperature-mediated feedback that is significantly more negative (Fig.
 563 A2a). Furthermore, we also check the results by applying the method of CMH16
 564 to our cloud histograms and kernels. This yields a mean temperature-mediated
 565 feedback of $-0.49 \pm 0.82 \text{ Wm}^{-2}\text{K}^{-1}$ between 45° - 60° S relative to local warming
 566 between 500-850 hPa, which is consistent with the value of $-0.76 \pm 0.82 \text{ Wm}^{-2}\text{K}^{-1}$
 567 reported by CMH16. This result shows that the treatment of confounding
 568 meteorological factors is likely the main reason for the discrepancy among the
 569 studies.

570 The relative importance of different confounding meteorological factors
 571 can be estimated based on their correlation with temperature. For a given
 572 MODIS histogram bin i , a confounding meteorological variable x_i will bias the
 573 estimate of the temperature-mediated cloud-feedback from the temperature-only
 574 regression model by an amount F_{SW,x_i} given by

$$575 \quad F_{SW,x_i} = \frac{\partial c_i}{\partial x_i} \frac{dx_i}{dT_i} K_i \frac{dT_i}{dT_{2m}}.$$

576 Based on this relationship, we find that estimated inversion strength and
 577 meridional wind are the two most important confounding factors. Failure to
 578 control for these variables will significantly bias the estimate of the overall
 579 temperature-mediated cloud feedback and potentially introduce a sign error.
 580 Thus, in our view, the feedback estimates of CMH16 are not reliable.

581

582 *Time Period*

583 Our analysis assumes that extratropical cloud-temperature relationships
 584 will not substantially change as the climate responds to anthropogenic radiative
 585 forcing. This assumption has been verified in many model projections of
 586 anthropogenic climate change (Gordon and Klein, 2014; Terai et al., 2016;
 587 Ceppi, McCoy, and Hartmann, 2016), though it does not hold in every model
 588 (Bjordal et al., 2020). To check the assumption further, we compare temperature-
 589 mediated feedbacks inferred from the first eight years (2003-2010) and the final
 590 eight years (2012-2019) of the 17-year MODIS record. The feedbacks inferred
 591 from the two periods are similar to one another and to the main estimate (Fig.

592 A2b). This provides some additional support for the assumption of time-invariant
593 cloud-temperature relationships, at least for decadal climate changes.

594

595 *Observing Platform*

596 Our main analysis infers feedbacks using MODIS data from the Aqua
597 satellite. We also check the results using MODIS data from the Terra satellite
598 because MODIS-Terra is calibrated differently and acquires data in the morning
599 rather than the afternoon. The temperature-mediated feedbacks inferred from
600 MODIS-Aqua and MODIS-Terra are similar, so the results are not sensitive to the
601 observing platform (Fig. A2c).

602

603 *Solar Zenith Angle Bias*

604 In addition to temporal sampling limitations, MODIS data have systematic
605 biases that occur during certain conditions. The first bias we consider is
606 associated with solar zenith angle (SZA). MODIS cloud retrievals assume that
607 radiative transfer is plane parallel and that each pixel is unaffected by the
608 radiative transfer in its surroundings. These assumptions break down when SZA
609 $> 65^\circ$, which biases the cloud data (Grosvenor and Wood, 2014). We investigate
610 this bias by screening the data based on SZA. Latitude-month combinations are
611 considered to have “good” data if $\text{SZA} < 65^\circ$ at the data acquisition time for all
612 pixel-level measurements, and latitude-month combinations are considered to
613 have “mixed” data otherwise. Sensitivity to SZA bias is checked by recalculating
614 the temperature-mediated feedback using only “good” data. Regression slopes
615 from latitude-month combinations with “mixed” data are replaced with regression
616 slopes from the same latitude and the closest calendar month with “good” data.
617 When two months are equally close, then their regression slopes are averaged.
618 The resulting feedback estimate is similar to the main estimate, indicating that
619 SZA bias does not influence the results (Fig. A2d). This is probably because the
620 bias does not affect data during spring and summer, when insolation is largest.

621

622 *Multilayer Clouds*

623 Other MODIS biases are especially relevant to the cloud-phase scattering
 624 feedback. For instance, the presence of multilayer clouds can cause errors in the
 625 retrievals of CTP and phase. We investigate this bias using the MODIS multilayer
 626 quality assurance flag, which identifies pixels that are suspected to be adversely
 627 affected by multilayer clouds. The proportion of cloudy scenes affected by
 628 multilayer clouds is

$$629 \quad M = N_{ML}/N_{cloud}$$

630 where N_{ML} is the number of pixels with potentially problematic multilayer clouds
 631 and N_{cloud} is the total number of cloudy pixels. For each latitude-calendar month
 632 pairing, high- M and low- M composites are created from data with above-median
 633 and below-median values of M , respectively. The cloud-phase scattering
 634 feedback is then estimated separately for the two composites. The M difference
 635 between the high and low composites is 2.4 times smaller than the mean value of
 636 M for the whole dataset, so the high- M -minus-low- M feedback difference is
 637 scaled by a factor of 2.4 to estimate the feedback bias from multilayer clouds.
 638 Even after applying the scaling factor, the high- M -minus-low- M difference is very
 639 small (Fig. A2e). Thus, multilayer clouds do not bias the estimate of cloud-phase
 640 scattering feedback.

641

642 *Liquid-topped Mixed-phase Clouds*

643 Another data limitation that is relevant to cloud-phase feedback is the fact
 644 that MODIS retrieves phase at cloud top, so it cannot distinguish liquid-topped
 645 mixed-phase (LTMP) clouds from pure liquid clouds. Our analysis therefore
 646 treats these clouds as a single phase category. If some LTMP clouds convert to
 647 pure-liquid clouds as they warm, then the associated feedback component would
 648 not be included in our estimate of cloud-phase scattering feedback. We therefore
 649 need to estimate this component using other methods.

650 LTMP clouds are investigated using MODIS data and radar-lidar data from
 651 the CloudSat and CALIPSO satellites. Footprint data are analyzed from the
 652 CloudSat MOD06-1KM-AUX and 2B-CLDCLASS-LIDAR datasets from June
 653 2006 through April 2011 (Sassen et al., 2008; Zhang et al., 2010). The radar-lidar

654 profiles detect phase below cloud top and label clouds as either “liquid”, “ice”, or
655 “mixed” phase. Each profile is matched with the collocated MODIS pixel and the
656 adjacent pixel on either side in the across-track direction. MODIS pixels are then
657 gridded by latitude, longitude, and month, and monthly cloud-fraction histograms
658 are calculated as a function of CTP, τ , and phase.

659 Although radar and lidar provide valuable information, they also have
660 sampling limitations that motivate minor methodological changes. Specifically,
661 the radar and lidar are nadir-staring instruments, so all of the collocated MODIS
662 pixels are viewed at nadir. These data differ from the full MODIS dataset
663 because of viewing angle dependencies (Maddux et al., 2010). Furthermore,
664 nadir sampling causes the number of MODIS pixels to vary by several orders of
665 magnitude between gridboxes, which is problematic for linear regression. We
666 accommodate this issue by calculating $\partial P_{liq}/\partial T$ by compositing. For each CTP-
667 latitude-calendar month combination, warm and cold composites are created
668 from the data with above-median and below-median temperature anomalies.
669 $\partial P_{liq}/\partial T$ is then calculated from the warm-minus-cold composite difference of the
670 mean values of P_{liq} and T weighted by the number of pixels in each gridbox.
671 Sampling uncertainty is then estimated by bootstrapping. Data are separated into
672 blocks with dimensions of 10° latitude, 10° longitude, and 1 month so that each
673 block has approximately one degree of freedom. Data blocks are randomly
674 selected with replacement to create 1000 bootstrap samples of the observations,
675 and cloud-phase scattering feedback is estimated from each sample. The 2.5
676 and 97.5 percentiles of the feedback values are used as bounds for the 95%
677 confidence interval associated with sampling uncertainty (Δ_1). All other aspects of
678 the cloud-phase feedback methodology are carried out as before.

679 Fig. A2f shows cloud-phase scattering feedback estimated by this method.
680 The first two cases show the effects of the methodological and viewing geometry
681 differences one at a time. The “Full FOV” case is the feedback estimated using
682 the full MODIS dataset and calculating $\partial P_{liq}/\partial T$ by compositing, and the “Nadir”
683 case is similar except that it uses near-nadir MODIS data that are collocated with
684 radar-lidar measurements. Feedbacks from these cases are statistically

685 indistinguishable from one another and from the main estimate. Thus, the
 686 differences in methodology and viewing geometry do not significantly affect the
 687 results.

688 Having established the “Nadir” feedback, we now leverage the radar-lidar
 689 data to distinguish pure-liquid clouds from LTMP clouds. MODIS pixels that
 690 coincide with radar-lidar data are assigned to one of three phase categories: (1)
 691 “ice” when MODIS reports ice, (2) “pure liquid” when MODIS reports liquid and
 692 radar-lidar reports that the highest liquid-containing cloud is pure liquid, and (3)
 693 “LTMP” when MODIS reports liquid and radar-lidar reports that the highest liquid-
 694 containing cloud is mixed phase or that all clouds are ice. The climatology of the
 695 cloud-fraction histograms for the three phases is shown in Fig. A3. As expected
 696 from previous work, pure-liquid clouds occur most often in the boundary layer,
 697 and LTMP clouds occur most often in the middle troposphere (Zhang et al., 2010;
 698 Mace et al., 2021).

699 The ability to distinguish pure-liquid and LTMP clouds facilitates a revised
 700 estimate of cloud-phase scattering feedback with three phase categories. For a
 701 given CTP bin, the proportion of total cloud fraction in each phase is:

$$702 \quad P_{ice} = \frac{C_{ice}}{C_{ice} + C_{pl} + C_{LTMP}}$$

$$703 \quad P_{pl} = \frac{C_{pl}}{C_{ice} + C_{pl} + C_{LTMP}}$$

$$704 \quad P_{LTMP} = \frac{C_{LTMP}}{C_{ice} + C_{pl} + C_{LTMP}}$$

705 where the subscripts “ice”, “pl”, and “LTMP” represent ice, pure liquid, and LTMP
 706 phases, respectively. We calculate $\partial C_{ice}/\partial T$, $\partial C_{pl}/\partial T$, and $\partial C_{LTMP}/\partial T$ and
 707 partition the values among the τ bins similarly to the main methodology. Finally,
 708 liquid condensate in LTMP clouds is assumed to be radiatively dominant over ice
 709 (Shupe et al., 2008), so the liquid-cloud kernel is used to calculate feedbacks for
 710 LTMP clouds. This method accounts for feedbacks that arise from phase
 711 transitions between any of the three categories, so it includes the component
 712 from LTMP-to-pure-liquid transitions that is missing from the main analysis.

713 The resulting feedback estimate is shown by the “Nadir w/ LTMP” case in
714 Fig. A2f. The estimate is consistent with the first two cases and with the main
715 estimate. Thus, the fact the MODIS is unable to distinguish LTMP clouds from
716 pure liquid clouds does not affect the main conclusions. The vertical separation
717 between LTMP and pure-liquid clouds is probably a key reason why the results
718 are not sensitive to the treatment of LTMP clouds (Fig. A3).

719

720 *Partly Cloudy Pixels*

721 The final data limitation we consider is the fact that MODIS excludes partly
722 cloudy pixels when compiling monthly histograms. This could introduce a
723 sampling bias if cloud elements that entirely cover pixels respond to warming
724 differently than cloud elements that partially cover pixels. Fully and partly cloudy
725 pixels make up 70.2% and 5.9% of the observations, respectively, and the partly
726 cloudy cases include 5.7% liquid clouds and 0.2% ice clouds. The partly cloudy
727 pixels are probably mostly associated with the edges of liquid clouds in the
728 boundary layer, where the estimated cloud-phase scattering feedback is small.
729 Thus, it is unlikely that excluding partly cloudy pixels affects the estimate of
730 cloud-phase scattering feedback.

731

732 **Acknowledgements**

733 We thank Tim Carlsen and Nick Lutsko for helpful discussions and Peter
734 Blossey for sharing the radiative transfer code. C.J.W. was supported by the
735 NOAA Climate and Global Change Postdoctoral Fellowship Program,
736 administered by UCAR's Cooperative Programs for the Advancement of Earth
737 System Science (CPAESS) under award #NA18NWS4620043B. C.J.W. and
738 J.R.N. were also supported by NASA under grant #80NSSC18K1020.

739

740 **Data and Code Availability**

741 The datasets used in this study include (1) MODIS Collection 6 versions
742 MYD08_M3 and MOD08_M3; (2) ERA5 reanalysis; (3) Clouds and the Earth's
743 Radiant Energy System (CERES) Energy Balanced and Filled Edition 4.1; (4)

744 CloudSat data products 2B-CLDCLASS-LIDAR and MOD06-1KM-AUX version
745 P1_R05; and (5) CMIP6 model output. These data are publicly available at
746 <https://earthdata.nasa.gov/>, <https://cds.climate.copernicus.eu/>,
747 <https://ceres.larc.nasa.gov/data/>, <http://www.cloudsat.cira.colostate.edu/>, and
748 <https://esgf-node.llnl.gov/projects/cmip6/>, respectively. The radiative transfer
749 model used in this study is available at http://rtweb.aer.com/rrtm_frame.html, and
750 the code for the climate-sensitivity analysis is available at
751 <https://doi.org/10.5281/zenodo.3945276>. MATLAB code used to process data is
752 available from the corresponding author upon request. The feedback estimates
753 are listed in Table S3 for reproducibility.

754 **References**

- 755 Armour, K., Marshall, J., Scott, J., Donohoe, A., & Newsom, E. R. (2016).
756 Southern Ocean warming delayed by circumpolar upwelling and
757 equatorward transport. *Nature Geoscience*, 9, 549–554.
758 <https://doi.org/10.1038/ngeo2731>
- 759 Betts, A. K., and Harshvardhan (1987). Thermodynamic constraint on the cloud
760 liquid water feedback in climate models, *Journal of Geophysical Research:*
761 *Atmospheres*, 92(D7), 8483– 8485, doi:10.1029/JD092iD07p08483
- 762 Bjordal, J., Storelvmo, T., Alterskjær, K., & Carlsen, T. (2020). Equilibrium
763 climate sensitivity above 5 °C plausible due to state-dependent cloud
764 feedback. *Nature Geoscience*, 13, 718–721.
765 <https://doi.org/10.1038/s41561-020-00649-1>
- 766 Bretherton, C. S., Widmann, M., Dymnikov, V. P., Wallace, J. M., & Bladé, I.
767 (1999). The Effective Number of Spatial Degrees of Freedom of a Time-
768 Varying Field. *Journal of Climate*, 12(7), 1990-2009.
769 [https://doi.org/10.1175/1520-0442\(1999\)012<1990:TENOSD>2.0.CO;2](https://doi.org/10.1175/1520-0442(1999)012<1990:TENOSD>2.0.CO;2)
- 770 Ceppi, P., & Hartmann, D. L. (2015). Connections Between Clouds, Radiation,
771 and Midlatitude Dynamics: a Review. *Current Climate Change*
772 *Reports*, 1, 94–102. <https://doi.org/10.1007/s40641-015-0010-x>
- 773 Ceppi, P., Hartmann, D. L., & Webb, M. J. (2016). Mechanisms of the Negative
774 Shortwave Cloud Feedback in Middle to High Latitudes. *Journal of*
775 *Climate*, 29(1), 139-157. <https://doi.org/10.1175/JCLI-D-15-0327.1>
- 776 Ceppi, P., McCoy, D. T., & Hartmann, D. L. (2016). Observational evidence for a
777 negative shortwave cloud feedback in middle to high latitudes. *Geophysical*
778 *Research Letters*, 43, 1331–1339, doi:10.1002/2015GL067499
- 779 Clough, S. A., Mlawer, E. J., Delamere, J. S., Iacono, M. J., Cady-Pereira, K.,
780 Boukabara, S., & Brown, P. D. (2004). Atmospheric radiative transfer
781 modeling: a summary of the AER codes. *Journal of Quantitative*
782 *Spectroscopy and Radiative Transfer*, 91, 233-244.
783 <https://doi.org/10.1016/j.jqsrt.2004.05.058>

- 784 Eastman, R., & Wood, R. (2018). The Competing Effects of Stability and
785 Humidity on Subtropical Stratocumulus Entrainment and Cloud Evolution
786 from a Lagrangian Perspective, *Journal of the Atmospheric Sciences*, 75(8),
787 2563-2578. <https://doi.org/10.1175/JAS-D-18-0030.1>
- 788 Ebert, E. E., & Curry, J. A. (1992). A parameterization of ice cloud optical
789 properties for climate models. *Journal of Geophysical Research:*
790 *Atmospheres*, 97(D4), 3831–3836, doi:10.1029/91JD02472
- 791 Frey, W. R., & Kay, J. E. (2018). The influence of extratropical cloud phase and
792 amount feedbacks on climate sensitivity. *Climate Dynamics*, 50, 3097–3116
793 <https://doi.org/10.1007/s00382-017-3796-5>
- 794 Fu, Q. (1996). An Accurate Parameterization of the Solar Radiative Properties of
795 Cirrus Clouds for Climate Models. *Journal of Climate*, 9(9), 2058-2082.
796 [https://doi.org/10.1175/1520-0442\(1996\)009<2058:AAPOTS>2.0.CO;2](https://doi.org/10.1175/1520-0442(1996)009<2058:AAPOTS>2.0.CO;2)
- 797 Gordon, N. D., & Klein, S. A. (2014). Low-cloud optical depth feedback in climate
798 models. *Journal of Geophysical Research: Atmospheres*, 119, 6052– 6065,
799 doi:10.1002/2013JD021052
- 800 Gregory, J. M., Ingram, W. J., Palmer, M. A., Jones, G. S., Stott, P. A., Thorpe,
801 R. B., et al. (2004). A new method for diagnosing radiative forcing and
802 climate sensitivity. *Geophysical Research Letters*, 31, L03205,
803 doi:10.1029/2003GL018747
- 804 Grosvenor, D. P. & Wood, R. (2014). The effect of solar zenith angle on MODIS
805 cloud optical and microphysical retrievals within marine liquid water clouds.
806 *Atmospheric Chemistry and Physics*, 14, 7291–7321,
807 <https://doi.org/10.5194/acp-14-7291-2014>
- 808 Hartmann, D. L. (2016). *Global Physical Climatology Second Edition*. Academic
809 Press.
- 810 Hawcroft, M., Haywood, J. M., Collins, M., Jones, A., Jones, A. C., & Stephens,
811 G. (2017). Southern Ocean albedo, inter-hemispheric energy transports and
812 the double ITCZ: global impacts of biases in a coupled model. *Climate*
813 *Dynamics* 48, 2279–2295. <https://doi.org/10.1007/s00382-016-3205-5>

- 814 Haynes, J. M., Jakob, C., Rossow, W. B., Tselioudis, G., & Brown, J. (2011).
815 Major Characteristics of Southern Ocean Cloud Regimes and Their Effects
816 on the Energy Budget. *Journal of Climate*, 24(19), 5061-5080.
817 <https://doi.org/10.1175/2011JCLI4052.1>
- 818 Hersbach, H., Bell, B., Berrisford, P., Hirahara, S., Horányi, A., Muñoz-Sabater,
819 J., et al. (2020). The ERA5 global reanalysis. *Quarterly Journal of the Royal
820 Meteorological Society*, 146, 1999– 2049. <https://doi.org/10.1002/qj.3803>
- 821 Huang, Y., Siems, S. T., Manton, M. J., Rosenfeld, D., Marchand, R.,
822 McFarquhar, G. M., & Protat, A. (2016). What is the Role of Sea Surface
823 Temperature in Modulating Cloud and Precipitation Properties over the
824 Southern Ocean? *Journal of Climate*, 29(20), 7453-7476.
825 <https://doi.org/10.1175/JCLI-D-15-0768.1>
- 826 Hwang, Y. T., & Frierson, D. M. W. (2013). Link between the double-Intertropical
827 Convergence Zone problem and cloud biases over the Southern Ocean.
828 *Proceedings of the National Academy of Sciences of the U.S.A.* 110(13),
829 4935–4940. <https://doi.org/10.1073/pnas.1213302110>
- 830 Jeevanjee, N., & Fueglistaler, S. (2020). Simple Spectral Models for Atmospheric
831 Radiative Cooling. *Journal of the Atmospheric Sciences*, 77(2), 479-
832 497. <https://doi.org/10.1175/JAS-D-18-0347.1>
- 833 Kay, J. E., Wall, C. J., Yettella, V., Medeiros, B., Hannay, C., Caldwell, P., & Bitz,
834 C. (2016). Global Climate Impacts of Fixing the Southern Ocean Shortwave
835 Radiation Bias in the Community Earth System Model (CESM). *Journal of
836 Climate*, 29(12), 4617-4636. <https://doi.org/10.1175/JCLI-D-15-0358.1>
- 837 Loeb, N. G., Doelling, D. R., Wang, H., Su, W., Nguyen, C., Corbett, J. G., et al.
838 (2018). Clouds and the Earth's Radiant Energy System (CERES) Energy
839 Balanced and Filled (EBAF) Top-of-Atmosphere (TOA) Edition-4.0 Data
840 Product. *Journal of Climate*, 31(2), 895-918. [https://doi.org/10.1175/JCLI-D-
17-0208.1](https://doi.org/10.1175/JCLI-D-
841 17-0208.1)
- 842 Lutsko, N. J. & Cronin, T. W. (2018). Increase in precipitation efficiency with
843 surface warming in radiative-convective equilibrium. *Journal of Advances in*

- 844 *Modeling Earth Systems*, 10, 2992– 3010.
845 <https://doi.org/10.1029/2018MS001482>
- 846 Lutsko, N. J., Popp, M., Nazarian, R. H., & Albright, A. L. (2021). Emergent
847 constraints on regional cloud feedbacks. *Geophysical Research Letters*, 48,
848 e2021GL092934. <https://doi.org/10.1029/2021GL092934>
- 849 Mace, G. G., Protat, A., Humphries, R. S., Alexander, S. P., McRobert, I.
850 M., Ward, J., et al. (2021). Southern Ocean cloud properties derived from
851 CAPRICORN and MARCUS data. *Journal of Geophysical Research:*
852 *Atmospheres*, 126, e2020JD033368. <https://doi.org/10.1029/2020JD033368>
- 853 Maddux, B. C., Ackerman, S. A., & Platnick, S. (2010). Viewing Geometry
854 Dependencies in MODIS Cloud Products. *Journal of Atmospheric and*
855 *Oceanic Technology*, 27(9), 1519-1528.
856 <https://doi.org/10.1175/2010JTECHA1432.1>
- 857 Marchant, B., Platnick, S., Meyer, K., Arnold, G. T., & Riedi, J. (2016). MODIS
858 Collection 6 shortwave-derived cloud phase classification algorithm and
859 comparisons with CALIOP. *Atmospheric Measurement Techniques*, 9,
860 1587–1599, <https://doi.org/10.5194/amt-9-1587-2016>
- 861 McCoy, D. T., Field, P., Bodas-Salcedo, A., Elsaesser, G. S., & Zelinka, M. D.
862 (2020). A Regime-Oriented Approach to Observationally Constraining
863 Extratropical Shortwave Cloud Feedbacks. *Journal of Climate*, 33(23),
864 9967-9983. <https://doi.org/10.1175/JCLI-D-19-0987.1>
- 865 McCoy, D. T., Hartmann, D. L., & Grosvenor, D. P. (2014a). Observed Southern
866 Ocean Cloud Properties and Shortwave Reflection. Part I: Calculation of
867 SW Flux from Observed Cloud Properties, *Journal of Climate*, 27(23), 8836-
868 8857. <https://doi.org/10.1175/JCLI-D-14-00287.1>
- 869 McCoy, D. T., Hartmann, D. L., & Grosvenor, D. P. (2014b). Observed Southern
870 Ocean Cloud Properties and Shortwave Reflection. Part II: Phase Changes
871 and Low Cloud Feedback. *Journal of Climate*, 27(23), 8858-8868.
872 <https://doi.org/10.1175/JCLI-D-14-00288.1>
- 873 Mülmenstädt, J., Salzmann, M., Kay, J. E., Zelinka, M. D., Ma, P., Nam, C., et al.
874 (2021). An underestimated negative cloud feedback from cloud lifetime

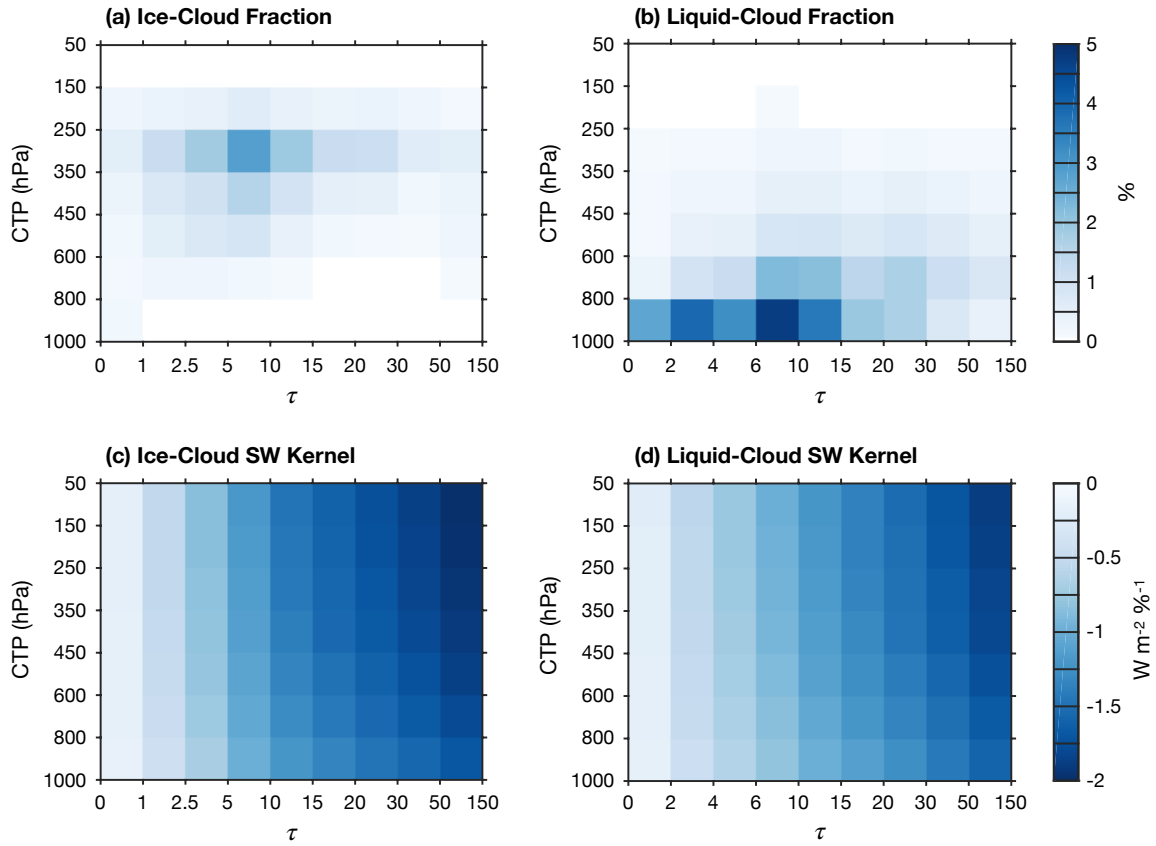
- 875 changes. *Nature Climate Change*, 11, 508–513.
876 <https://doi.org/10.1038/s41558-021-01038-1>
- 877 Myers, T. A., Scott, R. C., Zelinka, M. D., Klein, S. A., Norris, J. R., & Caldwell, P.
878 M. (2021). Observational constraints on low cloud feedback reduce
879 uncertainty of climate sensitivity. *Nature Climate Change*, 11, 501–507.
880 <https://doi.org/10.1038/s41558-021-01039-0>
- 881 Norris, J. R., & Iacobellis, S. F. (2005). North Pacific Cloud Feedbacks Inferred
882 from Synoptic-Scale Dynamic and Thermodynamic Relationships. *Journal*
883 *of Climate*, 18(22), 4862-4878. <https://doi.org/10.1175/JCLI3558.1>
- 884 Platnick, S., Meyer, K., King, M. D., Wind, G., Amarasinghe, N., Marchant, B., et
885 al. (2017). The MODIS Cloud Optical and Microphysical Products:
886 Collection 6 Updates and Examples From Terra and Aqua. *IEEE*
887 *Transactions on Geoscience and Remote Sensing*, 55(1), 502-525,
888 doi:10.1109/TGRS.2016.2610522
- 889 Sassen, K., Wang, Z., & Liu, D. (2008). Global distribution of cirrus clouds from
890 CloudSat/Cloud-Aerosol Lidar and Infrared Pathfinder Satellite
891 Observations (CALIPSO) measurements. *Journal of Geophysical Research:*
892 *Atmospheres*, 113, D00A12, doi:10.1029/2008JD009972
- 893 Scott, R. C., Myers, T. A., Norris, J. R., Zelinka, M. D., Klein, S. A., Sun, M., &
894 Doelling, D. R. (2020). Observed Sensitivity of Low-Cloud Radiative Effects
895 to Meteorological Perturbations over the Global Oceans. *Journal of*
896 *Climate*, 33(18), 7717-7734. <https://doi.org/10.1175/JCLI-D-19-1028.1>
- 897 Sherwood, S. C., Webb, M. J., Annan, J. D., Armour, K. C., Forster, P.
898 M., Hargreaves, J. C., et al. (2020). An assessment of Earth's climate
899 sensitivity using multiple lines of evidence. *Reviews of Geophysics*. 58,
900 e2019RG000678. <https://doi.org/10.1029/2019RG000678>
- 901 Shupe, M. D., Daniel, J. S., de Boer, G., Eloranta, E. W., Kollias, P., Long, C. N.,
902 et al. (2008). A Focus On Mixed-Phase Clouds, *Bulletin of the American*
903 *Meteorological Society*, 89(10), 1549-1562.
904 <https://doi.org/10.1175/2008BAMS2378.1>

- 905 Stackhouse, P. W., Jr., & Stephens, G. L. (1991). A Theoretical and
906 Observational Study of the Radiative Properties of Cirrus: Results from
907 FIRE 1986. *Journal of Atmospheric Sciences*, 48(18), 2044-2059.
908 [https://doi.org/10.1175/1520-0469\(1991\)048<2044:ATAOSO>2.0.CO;2](https://doi.org/10.1175/1520-0469(1991)048<2044:ATAOSO>2.0.CO;2)
- 909 Storelvmo, T., Tan, I., & Korolev, A. V. (2015). Cloud Phase Changes Induced by
910 CO₂ Warming—a Powerful yet Poorly Constrained Cloud-Climate
911 Feedback. *Current Climate Change Reports*, 1, 288–296.
912 <https://doi.org/10.1007/s40641-015-0026-2>
- 913 Tan, I., Oreopoulos, L., & Cho, N. (2019). The role of thermodynamic phase
914 shifts in cloud optical depth variations with temperature. *Geophysical
915 Research Letters*, 46, 4502– 4511. <https://doi.org/10.1029/2018GL081590>
- 916 Tan, I., Storelvmo, T., & Zelinka, M. D. (2016). Observational constraints on
917 mixed-phase clouds imply higher climate sensitivity. *Science*, 352, 224-227.
918 [doi:10.1126/science.aad5300](https://doi.org/10.1126/science.aad5300)
- 919 Terai, C. R., Zelinka, M., & Klein, S. A. (2016). Constraining the low-cloud optical
920 depth feedback at middle and high latitudes using satellite observations.
921 *Journal of Geophysical Research: Atmospheres*, 121, 9696–9716,
922 [doi:10.1002/2016JD025233](https://doi.org/10.1002/2016JD025233)
- 923 Terai, C. R., Zhang, Y., Klein, S. A., Zelinka, M. D., Chiu, J. C., & Min,
924 Q. (2019). Mechanisms behind the extratropical stratiform low-cloud optical
925 depth response to temperature in ARM site observations, *Journal of
926 Geophysical Research: Atmospheres*, 124, 2127–
927 2147. <https://doi.org/10.1029/2018JD029359>
- 928 Thompson, D. W. J., Bony, S., & Li, W. (2017). Thermodynamic constraint on the
929 depth of the global tropospheric circulation. *Proceedings of the National
930 Academy of Sciences of the USA*, 114, 8181-8186.
931 <https://doi.org/10.1073/pnas.1620493114>
- 932 Trenberth, K. E., & Fasullo, J. T. (2010). Simulation of Present-Day and Twenty-
933 First-Century Energy Budgets of the Southern Oceans. *Journal of
934 Climate*, 23(2), 440-454. <https://doi.org/10.1175/2009JCLI3152.1>

- 935 Tselioudis, G., DelGenio, A. D., Kovari, W., Jr., & Yao, M. (1998). Temperature
936 Dependence of Low Cloud Optical Thickness in the GISS GCM:
937 Contributing Mechanisms and Climate Implications. *Journal of*
938 *Climate*, 11(12), 3268-3281. [https://doi.org/10.1175/1520-](https://doi.org/10.1175/1520-0442(1998)011<3268:TDOLCO>2.0.CO;2)
939 [0442\(1998\)011<3268:TDOLCO>2.0.CO;2](https://doi.org/10.1175/1520-0442(1998)011<3268:TDOLCO>2.0.CO;2)
- 940 Tselioudis, G., Rossow, W. B., & Rind, D. (1992). Global Patterns of Cloud
941 Optical Thickness Variation with Temperature, *Journal of Climate*. 5(12),
942 1484-1495. [https://doi.org/10.1175/1520-](https://doi.org/10.1175/1520-0442(1992)005<1484:GPOCOT>2.0.CO;2)
943 [0442\(1992\)005<1484:GPOCOT>2.0.CO;2](https://doi.org/10.1175/1520-0442(1992)005<1484:GPOCOT>2.0.CO;2)
- 944 Wood, R., & Bretherton, C. S. (2006). On the Relationship between Stratiform
945 Low Cloud Cover and Lower-Tropospheric Stability. *Journal of*
946 *Climate*, 19(24), 6425-6432. <https://doi.org/10.1175/JCLI3988.1>
- 947 Zelinka, M. D., Klein, S. A., & Hartmann, D. L. (2012). Computing and
948 Partitioning Cloud Feedbacks Using Cloud Property Histograms. Part I:
949 Cloud Radiative Kernels. *Journal of Climate*, 25(11), 3715-3735.
950 <https://doi.org/10.1175/JCLI-D-11-00248.1>
- 951 Zelinka, M. D., Myers, T. A., McCoy, D. T., Po-Chedley, S., Caldwell, P.
952 M., Ceppi, P., et al. (2020). Causes of higher climate sensitivity in CMIP6
953 models. *Geophysical Research Letters*, 47, e2019GL085782.
954 <https://doi.org/10.1029/2019GL085782>
- 955 Zhang, D., Wang, Z., & Liu, D. (2010). A global view of midlevel liquid-layer
956 topped stratiform cloud distribution and phase partition from CALIPSO and
957 CloudSat measurements. *Journal of Geophysical Research:*
958 *Atmospheres*, 115, D00H13, doi:10.1029/2009JD012143

959 **Figures**

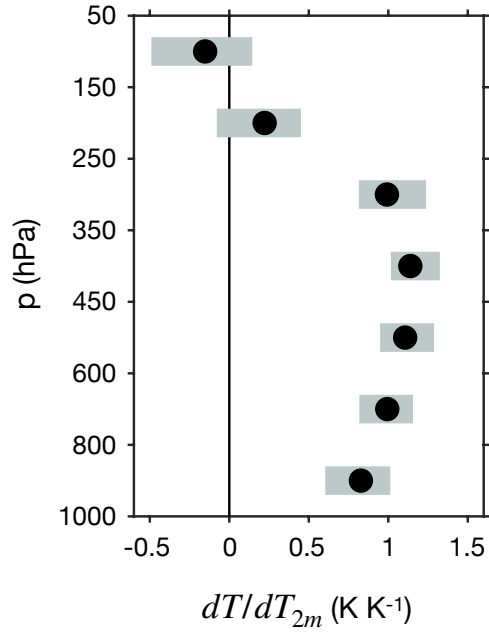
960



961

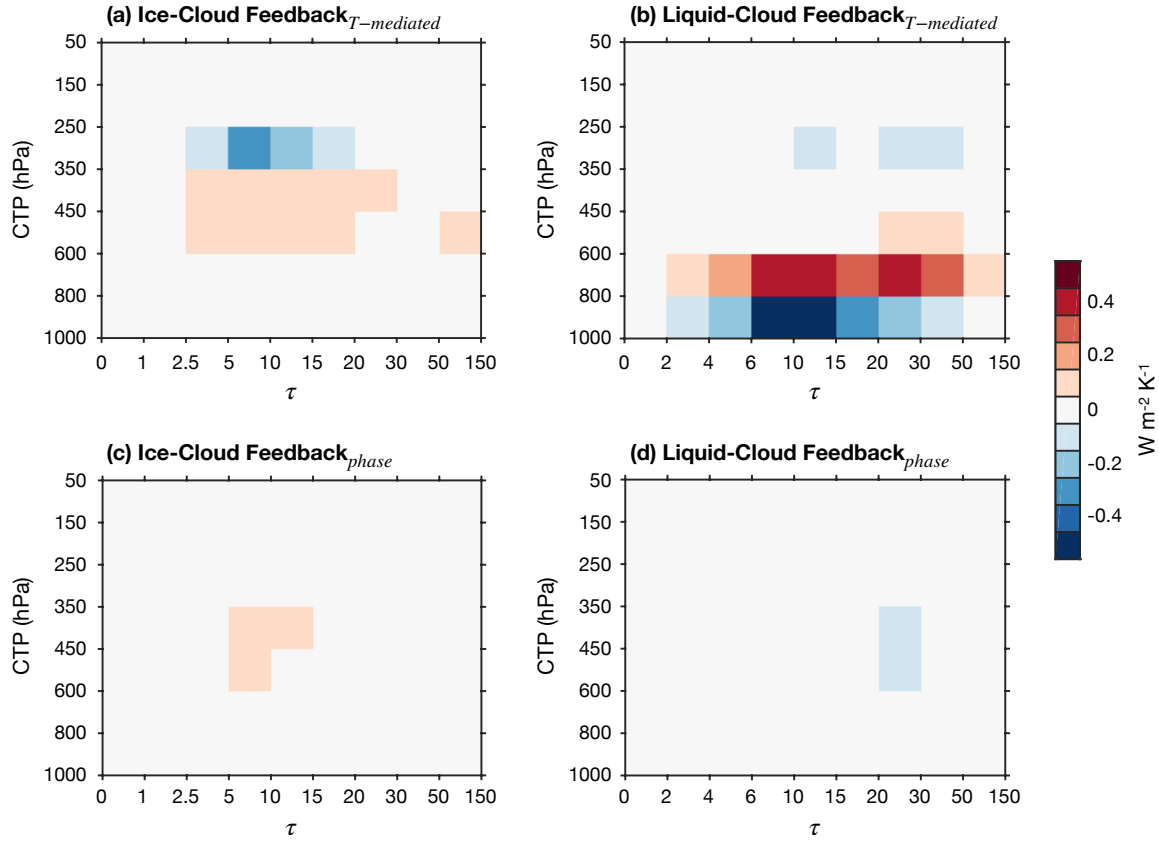
962

963 **Figure 1.** Climatology of cloud fraction and SW cloud radiative kernels over the
 964 Southern Ocean. Ice- and liquid-cloud fraction are shown in (a-b), and the ice-
 965 and liquid-cloud kernels are shown in (c-d).



966

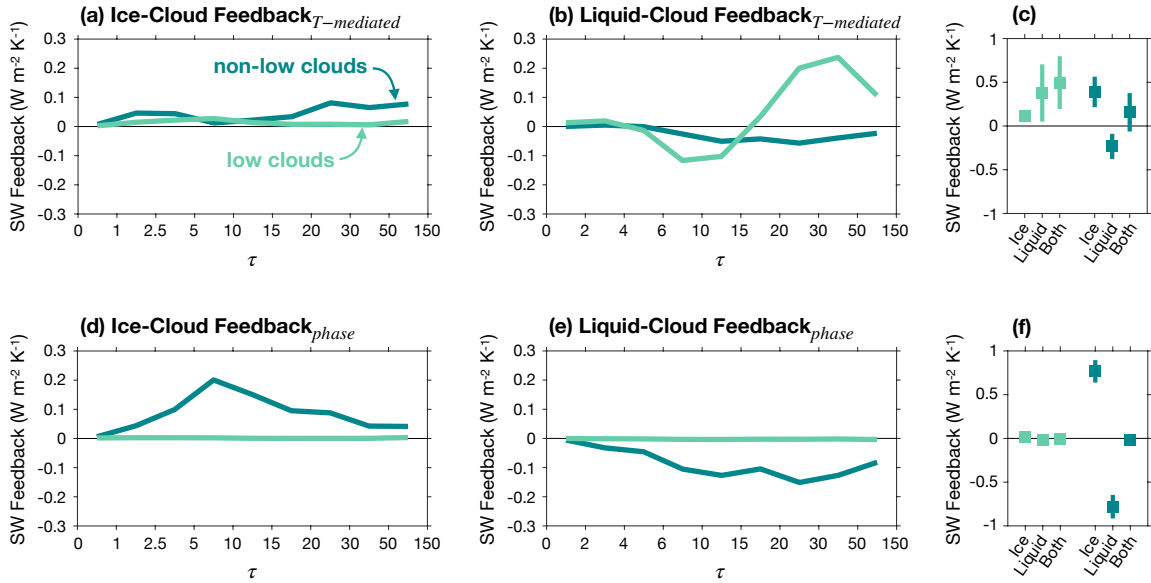
967 **Figure 2.** Ratio of atmospheric warming over the Southern Ocean to global-
 968 mean surface warming from CMIP6 projections forced by increasing atmospheric
 969 CO₂ (dT/dT_{2m}). The plotted values are spatial and temporal averages. Black
 970 dots show the multi-model mean, and gray bars show the inter-model range.



971

972

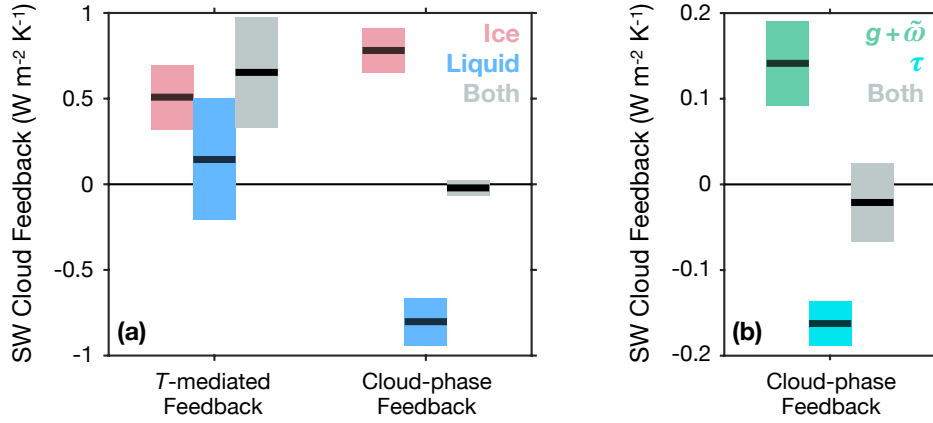
973 **Figure 3.** Southern Ocean SW cloud feedback as a function of cloud-top
 974 pressure (CTP), optical depth (τ), and phase. The temperature-mediated
 975 feedback is shown in (a-b), and the cloud-phase scattering feedback is shown in
 976 (c-d).



977

978

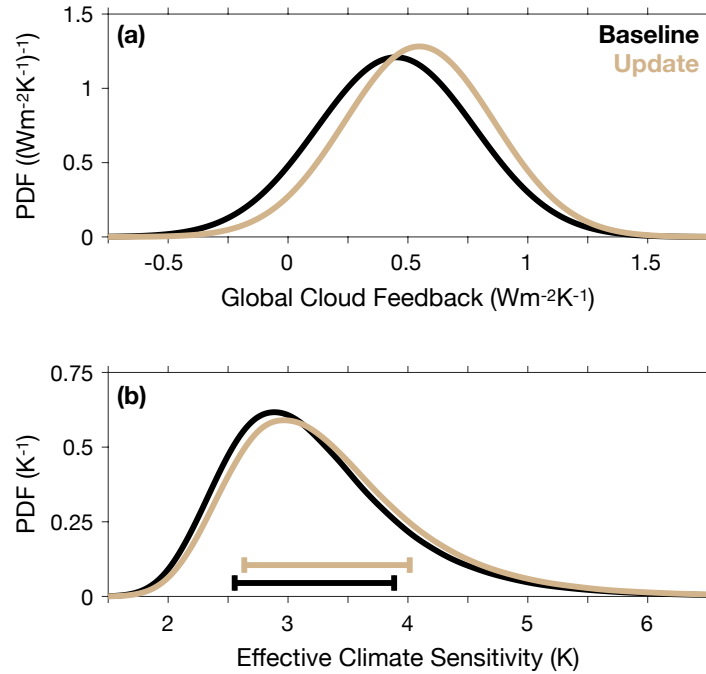
979 **Figure 4.** SW feedbacks from low clouds (CTP > 600 hPa) and non-low clouds
 980 (CTP ≤ 600 hPa). (a-b) Ice- and liquid-cloud components of the temperature-
 981 mediated feedback as a function of optical depth (τ). (c) Feedback components
 982 summed over the τ dimension. The sum of the liquid- and ice-cloud components
 983 is labeled “Both”. Squares and lines show the mean and 95% confidence interval.
 984 (d-f) As in (a-c), but for the cloud-phase scattering feedback.



985

986

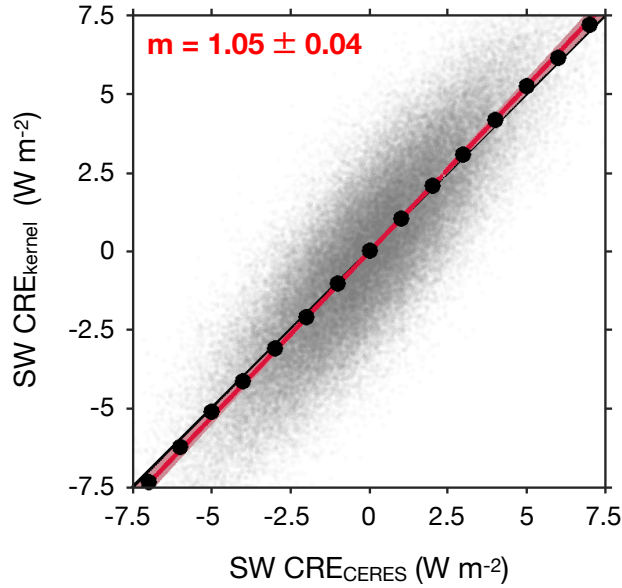
987 **Figure 5.** Mean SW cloud feedback over the Southern Ocean. (a) Temperature-
 988 mediated feedback and cloud-phase scattering feedback for ice clouds, liquid
 989 clouds, and both phases combined. Lines and colored bars show the mean and
 990 95% confidence interval. (b) Cloud-phase scattering feedback decomposed into
 991 contributions from changes in cloud asymmetry parameter and single-scattering
 992 albedo ($g + \tilde{\omega}$) and optical depth (τ).



993

994

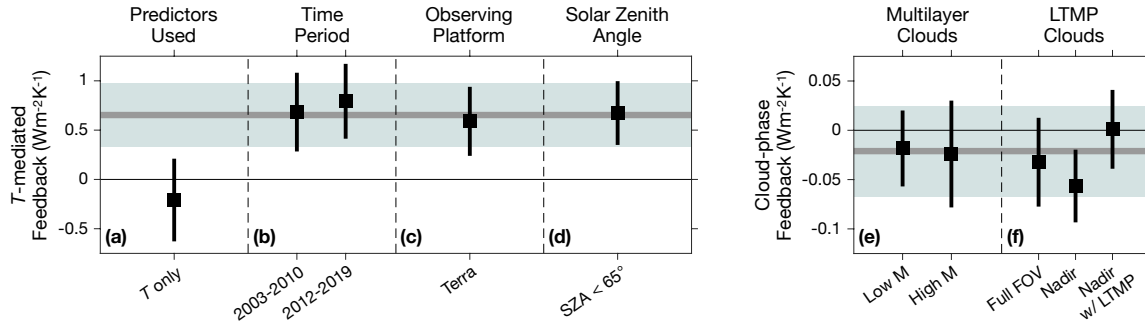
995 **Figure 6.** Implications of the feedback constraints for climate sensitivity. The
 996 “Baseline” case shows values from a survey by Sherwood et al. (2020), and the
 997 “Update” case is similar except that it uses our estimate of high-latitude low-cloud
 998 optical depth feedback. Probability density functions (PDF) are shown for (a)
 999 global cloud feedback and (b) effective climate sensitivity. Horizontal lines in (b)
 1000 show the 66% confidence range.



1001

1002

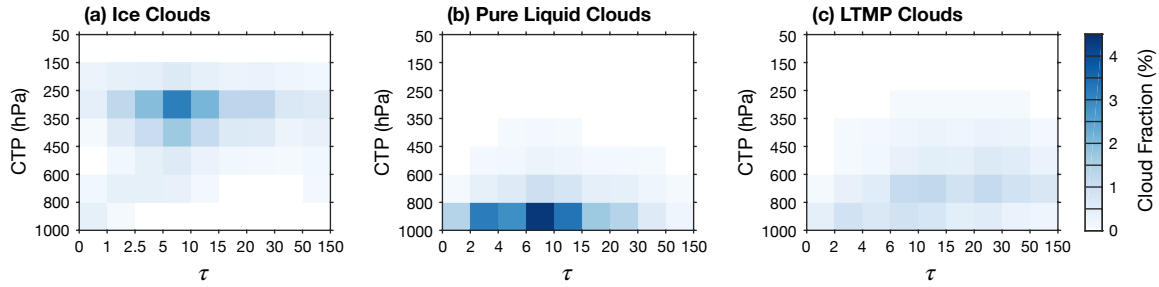
1003 **Figure A1.** Validation of the radiative kernels. Kernel-predicted SW cloud
1004 radiative effect (SW CRE_{kernel}) is plotted as function of observed SW cloud
1005 radiative effect (SW CRE_{CERES}). Grey dots are individual data points, and black
1006 dots are conditional means of SW CRE_{kernel} as a function of SW CRE_{CERES}. The
1007 red line and shading show the regression line and its 95% confidence interval.
1008 The regression slope is in the top left corner.



1009

1010

1011 **Figure A2.** Summary of the sensitivity tests. Panels (a-d) show the temperature-
 1012 mediated cloud feedback, and panels (e-f) show the cloud-phase scattering
 1013 feedback. The values represent feedbacks from all cloud phases combined. Gray
 1014 lines and shading show the mean and 95% confidence interval for the main
 1015 estimate, and black squares and lines show the mean and 95% confidence
 1016 interval for the sensitivity tests. (a) Sensitivity to excluding meteorological
 1017 predictors. The “*T* only” case estimates the feedback using only temperature as a
 1018 predictor. (b) Sensitivity to time period. The “2003-2010” and “2012-2019” cases
 1019 estimate feedbacks using the earliest and latest eight-year periods of the record.
 1020 (c) Sensitivity to observing platform. The “Terra” case estimates the feedback
 1021 using data from the Terra satellite. (d) Sensitivity to bias from high solar zenith
 1022 angle (SZA). The “SZA < 65°” case estimates the feedback using MODIS data
 1023 that are not affected by bias from high SZA. (e) Sensitivity to multilayer clouds.
 1024 The “Low M” and “High M” cases estimate feedbacks using subsets that have
 1025 relatively low and high proportions of data with suspected multilayer-cloud bias.
 1026 (f) Sensitivity to the treatment of liquid-topped mixed-phase clouds (LTMP). The
 1027 “Full FOV” case estimates the feedback using the full MODIS dataset and
 1028 applying the compositing technique that is introduced to accommodate radar-
 1029 lidar data (see text). The “Nadir” case is similar but uses the near-nadir subset of
 1030 MODIS pixels that are collocated with radar-lidar measurements. The “Nadir w/
 1031 LTMP” case is similar to the “Nadir” case except that the feedback is estimated
 1032 using three phase categories: “ice”, “pure liquid”, and “LTMP”.



1033

1034

1035 **Figure A3.** Climatology of cloud fraction over the Southern Ocean from MODIS
1036 data that are collocated with radar-lidar measurements from the CloudSat and
1037 CALIPSO satellites. Panels (a-c) show ice, pure liquid, and liquid-topped mixed-
1038 phase (LTMP) clouds, respectively.

**Supporting Information for “Observational Constraints on Southern Ocean
Cloud-phase Feedback”**

1 Casey J. Wall^{1*}, Trude Storelvmo^{2,3}, Joel R. Norris¹, Ivy Tan⁴

2 ¹Scripps Institution of Oceanography, University of California San Diego, La

3 Jolla, CA, United States

4 ²Department of Geosciences, University of Oslo, Oslo, Norway

5 ³School of Business, Nord University, Bodø, Norway

6 ⁴Department of Atmospheric and Oceanic Sciences, McGill University, Montreal,

7 Canada

8

9 Corresponding Author:

10 Casey J. Wall, cawall@ucsd.edu

11 **Contents of this file**

12 1. Text S1

13 2. Tables S1-S3

14

15 **Introduction**

16 This file includes an example of the procedure for estimating the scattering
 17 component of cloud-phase feedback (Text S1). It also contains tables that list the
 18 MODIS histogram bin boundaries (Table S1), the names of CMIP6 models
 19 analyzed in this study (Table S2), and the cloud-feedback estimates (Table S3).

20

21 **Text S1**

22 Here we show an example to illustrate the method for estimating the
 23 scattering component of cloud-phase feedback. The calculations are performed
 24 separately for each latitude, calendar month, and cloud-top pressure (CTP) bin,
 25 so we consider a single latitude-month-CTP combination from a hypothetical
 26 MODIS-like histogram. In this example the histogram has four optical depth (τ)
 27 bins for both liquid and ice clouds. Suppose that the climatological cloud fraction
 28 for the CTP-latitude-month combination is

$$29 \quad \overline{c_{liq}} = [2 \quad 2 \quad 4 \quad 1]$$

$$30 \quad \overline{c_{ice}} = [1 \quad 2 \quad 1 \quad 1]$$

31 in units of %. The climatological total liquid- and ice-cloud fractions are

$$32 \quad \overline{C_{liq}} = \sum_{k=1}^4 \overline{c_{liq,k}} = 9\%;$$

$$33 \quad \overline{C_{ice}} = \sum_{l=1}^4 \overline{c_{ice,l}} = 5\%.$$

34 The proportion of liquid cloud in the CTP bin, P_{liq} , is then regressed on the
 35 meteorological predictors. Suppose that the regression analysis finds that
 36 $\partial P_{liq}/\partial T = 0.04 \text{ } ^\circ\text{C}^{-1}$, where T is temperature in the CTP interval. The total liquid-
 37 and ice-cloud fraction changes arising from the cloud-phase scattering feedback
 38 are

$$39 \quad \frac{\partial C_{liq}}{\partial T} = \frac{\partial P_{liq}}{\partial T} (\overline{C_{liq}} + \overline{C_{ice}}) = (0.04 \text{ } ^\circ\text{C}^{-1})(9\% + 5\%) = 0.56\% \text{ } ^\circ\text{C}^{-1}$$

$$40 \quad \frac{\partial C_{ice}}{\partial T} = -\frac{\partial P_{liq}}{\partial T} (\overline{C_{liq}} + \overline{C_{ice}}) = -(0.04 \text{ } ^\circ\text{C}^{-1})(9\% + 5\%) = -0.56\% \text{ } ^\circ\text{C}^{-1}$$

41 The values of $\partial C_{liq}/\partial T$ and $\partial C_{ice}/\partial T$ are then partitioned among the τ bins in
42 proportion to the climatological τ distributions:

$$43 \quad \frac{\partial c_{liq}}{\partial T} = \frac{\partial C_{liq}}{\partial T} \frac{\overline{c_{liq}}}{\overline{C_{liq}}} = 0.56 \times \left[\frac{2}{9} \quad \frac{2}{9} \quad \frac{4}{9} \quad \frac{1}{9} \right] = [0.12 \quad 0.12 \quad 0.25 \quad 0.06]$$

$$44 \quad \frac{\partial c_{ice}}{\partial T} = \frac{\partial C_{ice}}{\partial T} \frac{\overline{c_{ice}}}{\overline{C_{ice}}} = -0.56 \times \left[\frac{1}{5} \quad \frac{2}{5} \quad \frac{1}{5} \quad \frac{1}{5} \right] = [-0.11 \quad -0.22 \quad -0.11 \quad -0.11]$$

45 where the units are $\% \text{ } ^\circ\text{C}^{-1}$. This procedure is repeated for every latitude-month-
46 CTP combination, and the results are multiplied by the radiative kernels and ratio
47 of local warming to global-mean surface warming (dT/dT_{2m}) to infer the cloud-
48 phase scattering feedback.

Histogram	CTP Bin Boundaries (hPa)	τ Bin Boundaries
Liquid Clouds - Original	50*, 250*, 300, 350, 400, 450, 500, 550, 600, 700, 800, 900, 1000**, 1100**	0, 2, 4, 6, 8, 10, 15, 20, 30, 40, 50, 100, 150
Liquid Clouds - Merged	50*, 150*, 250*, 350, 450, 600, 800**, 1000**	0, 2, 4, 6, 10, 15, 20, 30, 50, 150
Ice Clouds - Original	50, 100, 150, 200, 250, 300, 350, 400, 450, 500, 550, 600, 700, 800, 900, 1000**, 1100**	0, 0.5, 1, 2.5, 5, 7.5, 10, 15, 20, 30, 50, 100, 150
Ice Clouds - Merged	50, 150, 250, 350, 450, 600, 800**, 1000**	0, 1, 2.5, 5, 10, 15, 20, 30, 50, 150

49

50 **Table S1.** MODIS histogram bin boundaries. “Original” values are the standard
51 bin boundaries, and “Merged” values are the bin boundaries used in the analysis.

52 *It is assumed that no liquid clouds exist in the 50-150 hPa CTP interval, so the
53 50-250 hPa bin in the Original liquid-cloud histogram is assigned to the 150-250
54 hPa bin in the Merged histogram. **Clouds in the 1000-1100 hPa CTP bin of the
55 Original histogram are assigned to the 800-1000 hPa bin in the Merged
56 histogram.

ACCESS-CM2	CESM2-WACCM-FV2	GISS-E2-2-G	MRI-ESM2-0
ACCESS-ESM1-5	CIESM	IITM-ESM	NESM3
AWI-CM-1-1-MR	CMCC-CM2-SR5	INM-CM4-8	NorCPM1
CAMS-CSM1-0	EC-Earth3-AerChem	INM-CM5-0	NorESM2-LM
CanESM5	FGOALS-f3-L	IPSL-CM6A-LR	NorESM2-MM
CAS-ESM2-0	FGOALS-g3	MCM-UA-1-0	TaiESM1
CESM2	FIO-ESM-2-0	MIROC6	
CESM2-FV2	GISS-E2-1-G	MPI-ESM1-2-HR	
CESM2-WACCM	GISS-E2-1-H	MPI-ESM-1-2-HAM	

57

58 **Table S2.** CMIP6 models used in the analysis. Models are listed by their source
59 ID on the World Climate Research Programme CMIP6 archive ([https://esgf-
60 node.llnl.gov/projects/cmip6/](https://esgf-node.llnl.gov/projects/cmip6/)).

Feedback	Ice-cloud Component (Wm ⁻² K ⁻¹)	Liquid-cloud Component (Wm ⁻² K ⁻¹)	Both (Wm ⁻² K ⁻¹)	Figure
Temp.-mediated Feedback - Low Clouds	0.12 ± 0.02	0.38 ± 0.33	0.50 ± 0.30	Fig. 3c
Temp.-mediated Feedback - Non-low Clouds	0.39 ± 0.17	-0.23 ± 0.14	0.16 ± 0.22	Fig. 3c
Temp.-mediated Feedback - Total	0.51 ± 0.19	0.14 ± 0.36	0.65 ± 0.32	Fig. 4a
Cloud-phase Scattering Feedback - Low Clouds	0.01 ± 0.01	-0.02 ± 0.02	-0.007 ± 0.004	Fig. 3f
Cloud-phase Scattering Feedback - Non-low Clouds	0.77 ± 0.13	-0.78 ± 0.13	-0.01 ± 0.05	Fig. 3f
Cloud-phase Scattering Feedback - Total	0.78 ± 0.13	-0.80 ± 0.14	-0.02 ± 0.05	Fig. 4a
Feedback	$g + \tilde{\omega}$ Component (Wm ⁻² K ⁻¹)	τ Component (Wm ⁻² K ⁻¹)	Both (Wm ⁻² K ⁻¹)	Figure
Cloud-phase Scattering Feedback - Total	0.14 ± 0.05	-0.16 ± 0.03	-0.02 ± 0.05	Fig. 4b

61

62 **Table S3.** Components of Southern Ocean SW cloud feedback. Feedbacks are
63 spatially and temporally averaged over ice-free ocean between 40°-60°S. “Total”
64 indicates the sum of the low and non-low cloud components. The stated
65 uncertainty is the 95% confidence interval.